





# Surgical Planning and Optimization of Patient-Specific Fontan Grafts With Uncertain Post-Operative Boundary Conditions and Anastomosis Displacement

Xiaolong Liu , Narutoshi Hibino, Yue-Hin Loke, Byeol Kim, Paige Mass , Mark D. Fuge , Laura Olivieri, and Axel Krieger , *Member, IEEE*

**Abstract—Objective:** Fontan surgical planning involves designing grafts to perform optimized hemodynamic performance for the patient’s long-term health benefit. The uncertainty of post-operative boundary conditions (BC) and graft anastomosis displacements can significantly affect optimized graft designs and lead to undesirable outcomes, especially for hepatic flow distribution (HFD). We aim to develop a computation framework to automatically optimize patient-specific Fontan grafts with the maximized possibility of keeping post-operative results within clinical acceptable thresholds. **Methods:** The uncertainties of BC and anastomosis displacements were modeled using Gaussian distributions according to prior research studies. By parameterizing the Fontan grafts, we built surrogate models of hemodynamic parameters taking the design parameters and BC as input. A two-phase reliability-based robust optimization (RBRO) strategy was developed by combining deterministic optimization (DO) and optimization under uncertainty (OUU) to reduce computational cost. **Results:** We evaluated the performance of the RBRO framework by comparing it with the DO method in four cases of Fontan patients. The results showed that the surgical plans computed from the proposed method yield up to 79.2% improvement in the reliability of the HFD than those of the DO method ( $p < 0.0001$ ). The mean values of indexed power loss (iPL) and the percentage of non-physiologic wall shear

stress (%WSS) for the optimized surgical plans met the clinically acceptable thresholds. **Conclusion:** This study demonstrated the effectiveness of our RBRO framework to address the uncertainties of BC and anastomosis displacements for Fontan surgical planning. **Significance:** The technique developed in this paper demonstrates a significant improvement in the reliability of the predicted post-operative outcomes for Fontan surgical planning. This planning technique is immediately applicable as a building block to enable technology for optimal long-term outcomes for pediatric Fontan patients and can also be used in other pediatric and adult cardiac surgeries.

**Index Terms—**Design optimization, Fontan surgery, optimization under uncertainty, patient-specific vascular graft.

## I. INTRODUCTION

FONTAN surgery is the hallmark operation in the surgical management of patients with single ventricle congenital heart disease. To establish passive pulmonary blood flow, surgery involves directing systemic venous blood flow to the pulmonary artery (PA)<sup>1</sup> through vascular grafts bypassing the heart [1], [2]. The shape and implantation of Fontan grafts (Fig. 1), such as three-dimensional (3D) printed tissue engineered vascular grafts (TEVGs) [3] or commercially available grafts, can result in high indexed power loss (iPL) and an imbalanced hepatic flow distribution (HFD), which correlate with decreased exercise capacity [4] and pulmonary arteriovenous malformations (PAVM) [5], respectively.

Virtual planning of Fontan surgery as well as other types of cardiovascular surgery has shown great potential to predict post-operative hemodynamic outcome and help clinicians make better surgical plans by combining computer-aided design (CAD) [6], [7] and computational fluid dynamics (CFD) simulations [8]–[11]. To reduce manual effort and turnaround time for designing optimized patient-specific Fontan surgical plans with low iPLs and balanced HFDs, research efforts have been made to develop automatic design optimization techniques by parameterizing graft geometry, building surrogate functions of high-fidelity Fontan hemodynamics to reduce computation

Manuscript received 12 November 2021; revised 7 March 2022 and 23 April 2022; accepted 25 April 2022. Date of publication 27 April 2022; date of current version 20 October 2022. This work was supported in part by the National Institute of Health under Grants NHLBI-R01HL143468 and R21/R33HD090671, and in part by the TEDCO Maryland Innovation Initiative Award under Grant 1120-004. (*Corresponding author: Xiaolong Liu.*)

Xiaolong Liu is with the Department of Mechanical Engineering, Johns Hopkins University, Baltimore, MD 21218 USA (e-mail: xiaolong@jhu.edu).

Byeol Kim and Axel Krieger are with the Department of Mechanical Engineering, Johns Hopkins University, USA.

Narutoshi Hibino is with the Department of Surgery, The University of Chicago Medicine, USA.

Yue-Hin Loke and Laura Olivieri are with the Division of Cardiology, Children’s National Hospital, USA.

Paige Mass is with the Sheikh Zayed Institute for Pediatric Surgical Innovation, Children’s National Hospital, USA.

Mark D. Fuge is with the Department of Mechanical Engineering, University of Maryland, USA.

This article has supplementary downloadable material available at <https://doi.org/10.1109/TBME.2022.3170922>, provided by the authors.

Digital Object Identifier 10.1109/TBME.2022.3170922

<sup>1</sup>A list of nomenclatures are provided in the supplementary material.

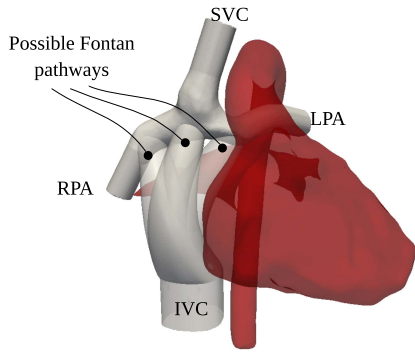


Fig. 1. Illustration of Fontan surgical planning. 3D reconstructed Fontan model with various possible Fontan pathways. Deoxygenated blood flow were directed from the superior vena cava (SVC) and the inferior vena cava (IVC) to the lungs via the left pulmonary artery (LPA) and the right pulmonary artery (RPA).

cost, and searching for graft parameters that can optimize objective functions, such as minimizing iPL or pursuing perfectly balanced HFD [12], [13]. However, the state-of-the-art Fontan surgical planning methodologies rely on the assumption that the post-operative boundary conditions (BC) are identical to the pre-operative BC. Previous studies [8], [14] show that the uncertainty of post-operative BC for Fontan surgical planning has a significant influence on the resulting HFD and may lead to highly unbalanced HFD despite well-balanced HFD in the pre-operative surgical plan. Furthermore, although surgeons can try their best to suture grafts according to optimized surgical plans, displacement of the anastomosis is unavoidable, which will also significantly affect post-operative HFD [12].

To address the challenge of tolerating the uncertainty of post-operative BC and anastomosis displacement, we develop a reliability-based robust optimization (RBRO) framework for patient-specific Fontan surgical planning and optimization of TEVG design based on our previous work [12]. In this work, we define the reliability and robustness of a Fontan surgical plan using  $P(\text{HFD}_{\text{balanced}})$  and  $\mathbb{E}(\text{iPL})$ , respectively.  $P(\text{HFD}_{\text{balanced}})$  represents the probability of 40%~60% post-operative hepatic flow to the left pulmonary artery (LPA), and  $\mathbb{E}(\text{iPL})$  represents the post-operative expectation of iPL under uncertainty. The RBRO framework is achieved by formulating a constrained optimization problem to find an optimal surgical plan (anastomosis location and angle) and graft shape design that can maximize  $P(\text{HFD}_{\text{balanced}})$  while constraining  $\mathbb{E}(\text{iPL})$  below the clinically acceptable threshold [15]. Furthermore, we also constrain the wall shear stress (WSS) [11] on the luminal surface of Fontan grafts to prevent graft designs begin inflated to disproportionate sizes.

The primary contributions of this work include:

- 1) We develop the RBRO computation framework of patient-specific Fontan graft planning for the first time to the best of our knowledge. It moves one important step towards providing surgeons a reliable tool for pre-operative Fontan surgical planning.
- 2) We study the effect of warm starting in the RBRO framework to improve computational efficiency while preserving the performance of optimal solutions by feeding initial

guesses of design parameters, which were computed from the DO solutions.

- 3) We demonstrate the effectiveness of the RBRO computation framework for Fontan surgical planning in four patient-specific models ( $n = 4$ ) by comparing the performance of Fontan grafts computed from the RBRO method with the performance of grafts obtained from the DO method.
- 4) We study how different objective functions in DO affect the warm-start graft designs and subsequently affect the RBRO results. The objective functions used in DO aim to compute graft designs with balanced HFD or minimized iPL.
- 5) We investigate how the RBRO framework works for Fontan patients with highly unbalanced PA flow splits to compute reliable surgical plans. We found that the framework tends to work better for pediatric patients than for adult patients.

## II. PROBLEM FORMULATION

### A. Research Objective

Given the patient-specific Fontan models, hemodynamic parameter optimization thresholds, and uncertainty models of BC and displacement of the anastomosis, our research objective is to automatically design Fontan grafts and anastomosis plans that maximize the possibility of having post-operative HFD within clinically acceptable thresholds.

### B. Hemodynamic Parameters and Optimization Thresholds

The hemodynamic performance of the Fontan pathway is defined by three parameters: 1) HFD; 2) iPL across the Fontan pathway; 3) the percentage of the Fontan surface area with non-physiologic wall shear stress, %WSS.

**1) Hepatic Flow Distribution HFD:** We use  $\text{HFD}_{\text{LPA}}$  to define HFD.  $\text{HFD}_{\text{LPA}}$  represents the ratio of blood flow from the IVC to the LPA and the total IVC flow.

**2) Indexed Power Loss iPL:** iPL is a dimensionless resistive index that correlates with exercise capacity [4]. It is calculated based on the patient's body surface area (BSA) and the absolute power loss (PL) between the total hemodynamic energy at the inlets (IVC, SVC) and the total hemodynamic energy at the outlets (LPA, RPA):

$$\text{iPL} = \frac{\text{BSA}^2}{\rho Q_s^2} \left[ \underbrace{\sum_I^{\text{SVC,IVC}} Q_I \left( \bar{p}_I + \frac{1}{2} \rho \bar{u}_I^2 \right) - \sum_O^{\text{LPA,RPA}} Q_O \left( \bar{p}_O + \frac{1}{2} \rho \bar{u}_O^2 \right)}_{\text{PL}} \right], \quad (1)$$

where the subscripts  $I$  and  $O$  represent inlets and outlets, respectively,  $Q_I$  and  $Q_O$  are the flow rates,  $\bar{p}_I$  and  $\bar{p}_O$  are the static pressures,  $\rho$  is the blood density, and  $\bar{u}_I$  and  $\bar{u}_O$  are the flow velocities.

**3) Percentage of Non-Physiologic Wall Shear Stress %WSS:** Oversized Fontan conduits can lead to low WSS that correlates with neointimal hyperplasia and thrombosis [16]. To prevent conduit oversizing, %WSS was introduced to measure the percentage of low WSS area on the luminal surface of Fontan conduits [11]:

$$\%WSS = \frac{\text{Area}_{\text{lowWSS}}}{\text{Area}_{\text{Conduit}}} \quad (2)$$

#### 4) Thresholds for Fontan Graft Optimization:

- $\text{HFD}_{\text{balanced}}$ :  $40\% < \text{HFD}_{\text{LPA}} < 60\%$ . The ideal HFD with 50% IVC flow to LPA is not always feasible. Based on Haggerty *et al.*'s computational fluid dynamics (CFD) study of hemodynamic parameters in 100 Fontan patients [15], the mean LPA split is 44% with an interquartile range of 31% to 57%. We aimed to have an acceptable HFD range to match this cohort of 40%~60%. In the following text, we use  $\text{HFD}_{\text{balanced}}$  to represent  $40\% < \text{HFD}_{\text{LPA}} < 60\%$ . The reliability of a Fontan surgical plan is represented by  $P(\text{HFD}_{\text{balanced}})$ , which is the probability of post-operative  $\text{HFD}_{\text{LPA}}$  within the range of 40%~60%.
- $i\text{PL} < 0.03$ . Based on [15], the mean  $i\text{PL}$  was 0.037 and the median  $i\text{PL}$  was 0.031. We set the  $i\text{PL}$  threshold at 0.03.
- $\%WSS < 10\%$ . The normal physiological range of WSS for venous flow is 1~10 dynes/cm<sup>2</sup> (0.1~1Pa) [17].  $\text{Area}_{\text{lowWSS}}$  in (2) represents the surface areas with WSS below 1 dynes/cm<sup>2</sup>. Setting 10% as the threshold, whilst arbitrary, did have a direct role in the CAD design process, which was demonstrated in our previous study [11]. Without %WSS, the generated Fontan conduits can be unacceptably large or oversized.

### C. Magnetic Resonance Imaging and Magnetic Resonance Angiography Flow Data Acquisition and Processing

This study was approved by the Institutional Review Boards (IRB) of all institutions with IRB Protocol Number Pro00013357. Cardiovascular magnetic resonance imaging (CMR) datasets from four patients who had undergone Fontan operation were anonymized and exported. Using angiography data with late-phase, non-gated, breath-held acquisition with pixel size  $1.4 \times 1.4$  mm, 3D anatomic replicas of Fontan and the proximal thoracic vasculature were created and phase contrast images were used to extract flow curves for the inlet and outlet BC for each patient.  $Q_{\text{SVC}}^m$ ,  $Q_{\text{IVC}}^m$ ,  $Q_{\text{LPA}}^m$  and  $Q_{\text{RPA}}^m$  represent time-averaged flow rates that were averaged over one cardiac cycle from CMR measurements, as shown in Fig. 2(A). For surgical planning, the original Fontan conduits were removed from the models shown in Fig. 3 to create a model of superior cavopulmonary connection (SCPC).

### D. Boundary Conditions

The preparation of the uncertain BC for Fontan virtual surgical planning with CFD simulations involves two steps: 1) calculate deterministic pre-operative BC  $Q_{\text{IVC}}$ ,  $Q_{\text{SVC}}$ ,  $Q_{\text{LPA}}$  and  $Q_{\text{RPA}}$ ; and

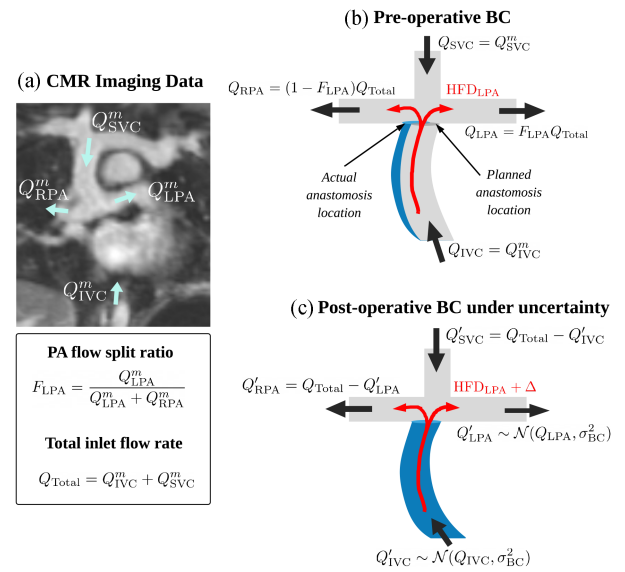


**Fig. 2.** Procedure of setting up uncertain BC for Fontan hemodynamic simulation. (A) Cardiovascular magnetic resonance (CMR) imaging for 3D cardiovascular structure reconstruction and blood flow rates measurement.  $Q_{\text{SVC}}^m$ ,  $Q_{\text{IVC}}^m$ ,  $Q_{\text{LPA}}^m$  and  $Q_{\text{RPA}}^m$  are time-averaged flow rates from CMR measurement.  $F_{\text{LPA}}$  and  $Q_{\text{Total}}$  represent PA flow split ratio and total inlet flow rate, respectively. (B)  $Q_{\text{SVC}}$ ,  $Q_{\text{IVC}}$ ,  $Q_{\text{LPA}}$  and  $Q_{\text{RPA}}$  are used for setting up deterministic Fontan hemodynamic simulation.  $\text{HFD}_{\text{LPA}}$  represents the hepatic flow distribution (HFD), which is the percentage of IVC flow to the LPA for the optimized graft at the planned anastomosis location. The blue graft shows the actual anastomosis location. (C)  $Q'_{\text{SVC}}$ ,  $Q'_{\text{IVC}}$ ,  $Q'_{\text{LPA}}$  and  $Q'_{\text{RPA}}$  are BC with introduced uncertainty.  $\text{HFD}_{\text{LPA}} + \Delta$  represents the change of HFD due to the uncertainties of the post-operative BC  $Q'_{\text{SVC}}$ ,  $Q'_{\text{IVC}}$ ,  $F'_{\text{LPA}}$  and the anastomosis displacement.

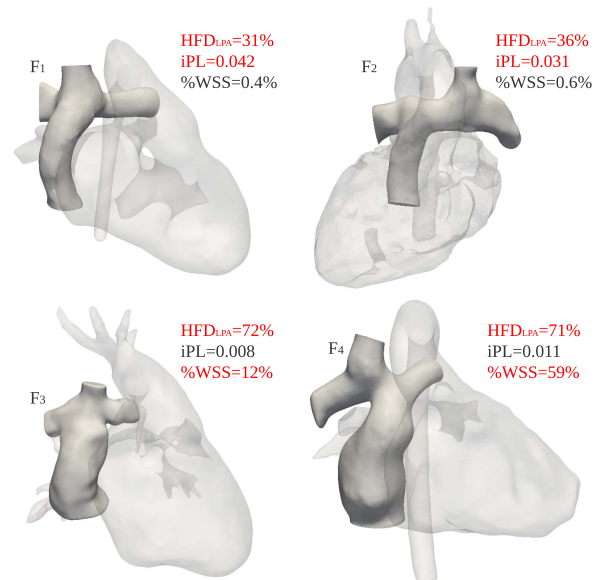


**Fig. 3.** 3D representation and hemodynamic results of original Fontans. A cohort of Fontan patients ( $n=4$ ) were retrospectively collected and digitally processed into 3D models for CFD simulation. The cohort consisted of 2 extracardiac-type Fontans ( $F_1$ ,  $F_2$ ), and 2 lateral tunnel-type Fontans ( $F_3$ ,  $F_4$ ). The original Fontan conduits were removed from the model for the surgical planning task. The highlighted hemodynamic parameters in red were considered outside the thresholds.

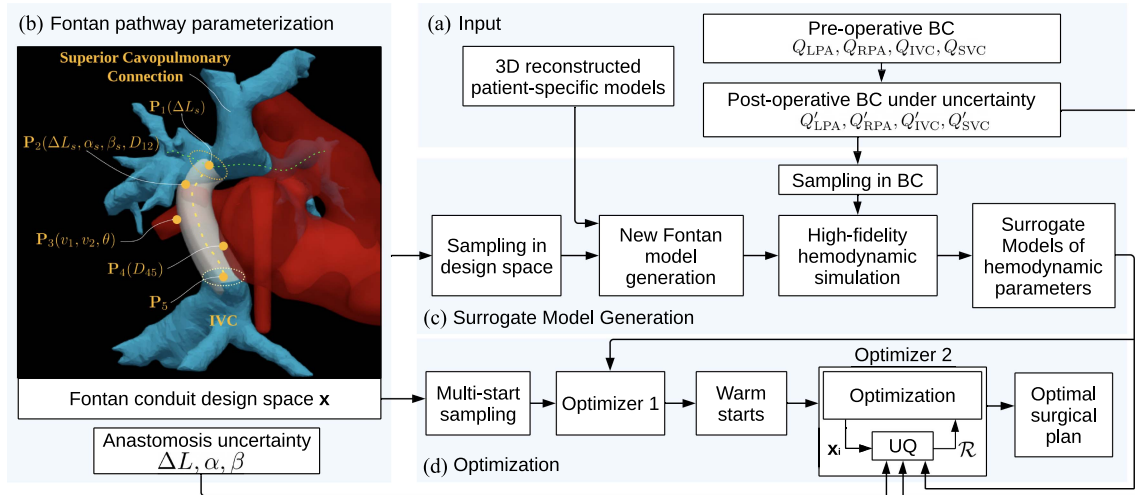


**Fig. 4.** Schematic of the RBRO computation framework. (A) The inputs of the framework include 3D Fontan models, the pre-operative BC, and the uncertainty models of BC. (B) Fontan pathway parameterization creates the design space  $\mathbf{x}$  for automatically exploring the conduit geometry, anastomosis location and orientation. The uncertainty models of anastomosis can also be considered as the inputs of the framework. (C) The surrogate model generation involves sampling in the design space and the space of uncertain parameters, computing the hemodynamic results, and applying Gaussian process regression to learn the hemodynamic responses of different inputs. (D) The RBRO optimization process includes two optimizers. The optimizer 1 performs DO to generate warm starts for the optimizer 2. The optimizer 2 performs OUU to compute the final optimal surgical plans.

2) add the post-operative BC uncertainty to the pre-operative BC as the final BC  $Q'_{IVC}$ ,  $Q'_{SVC}$ ,  $Q'_{LPA}$  and  $Q'_{RPA}$ .

The inlet flows  $Q_{IVC}$  and  $Q_{SVC}$  for pre-operative BC are identical to time-averaged CMR measured data  $Q_{IVC}^m$  and  $Q_{SVC}^m$ , as shown in Fig. 2(B). To maintain mass conservation, outlet flow rates  $Q_{LPA}$  and  $Q_{RPA}$  are prescribed as

$$Q_{LPA} = F_{LPA} Q_{Total}, \quad (3)$$

$$Q_{RPA} = (1 - F_{LPA}) Q_{Total}, \quad (4)$$

where the measured flow split ratio  $F_{LPA}$  is calculated by  $F_{LPA} = Q_{LPA}^m / Q_{Total}^m$ , and the total inlet flow rate (or cardiac output) is  $Q_{Total}^m = Q_{IVC}^m + Q_{SVC}^m$ . Patients with successful cardiovascular surgery are expected to restore their cardiac function in a short period of time. Therefore, it is reasonable to assume that the cardiac output  $Q_{Total}$  is similar after surgery. The pre-operative boundary conditions (BC) values for the patients are presented in the supplementary material (Table SI).

To estimate post-operative BC under uncertainty while preserving mass conservation, flow rates  $Q'_{LPA}$  and  $Q'_{IVC}$  are modeled assuming that short-term post-operative BC follow the Gaussian distribution [18], [19], as illustrated in Fig. 2(C). The pre-operative BC  $Q_{LPA}$  and  $Q_{IVC}$  are used as mean values of the Gaussian distribution for  $Q'_{LPA}$  and  $Q'_{IVC}$ . According to a previous study on comparing pre- and post-operative Fontan hemodynamics [14], we apply a maximal 20% change of  $Q_{LPA}$  and  $Q_{IVC}$  to derive the probability distributions of  $Q'_{LPA}$  and  $Q'_{IVC}$ :

$$P(Q_{LPA} - 20\%Q_{LPA} < Q'_{LPA} < Q_{LPA} + 20\%Q_{LPA}) \approx 99.7\%, \quad (5)$$

$$P(Q_{IVC} - 20\%Q_{IVC} < Q'_{IVC} < Q_{IVC} + 20\%Q_{IVC}) \approx 99.7\%, \quad (6)$$

where  $3\sigma_{LPA} = 20\%Q_{LPA}$  and  $3\sigma_{IVC} = 20\%Q_{IVC}$ .

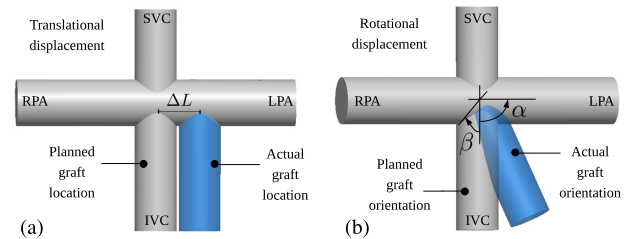


**Fig. 5.** Simplified Fontan models to illustrate the translational and rotational displacements. (A)  $\Delta L$  represents the uncertain translational displacement. (B)  $\alpha$  and  $\beta$  represent the uncertain rotational displacement.

Therefore, postoperative BC are formulated as follows:

$$Q'_{LPA} \sim \mathcal{N}(Q_{LPA}, \sigma_{LPA}^2), \quad (7)$$

$$Q'_{RPA} = Q_{Total} - Q'_{LPA}, \quad (8)$$

$$Q'_{IVC} \sim \mathcal{N}(Q_{IVC}, \sigma_{IVC}^2), \quad (9)$$

$$Q'_{SVC} = Q_{Total} - Q'_{IVC}, \quad (10)$$

where  $Q'_{RPA}$  depends on  $Q'_{LPA}$  and  $Q_{Total}$ ; and  $Q'_{SVC}$  depends on  $Q'_{IVC}$  and  $Q_{Total}$  to maintain mass conservation for the Fontan hemodynamic simulation.

### E. Anastomosis Uncertainty

Fig. 5(A) and 5(B) illustrate two types of displacement, i.e., translational displacement  $\Delta L$  and rotational displacement  $\alpha, \beta$ , respectively. The gray grafts represent the prescribed surgical plan, while the blue grafts demonstrate actual surgical implantation. The accuracy of graft implementation depends on the skill of the surgeon and assistive tools, such as paper rulers. Clinical data on surgical implantation accuracy are currently

unavailable. Based on the suggestion of our medical co-authors, we assume the maximum translational displacement as 5mm and the maximum rotational displacement as  $10^\circ$ . Gaussian distribution is used to model the anastomosis uncertainty:

$$P(\Delta L_s - 5 \text{ mm} < \Delta L < \Delta L_s + 5 \text{ mm}) \approx 99.7\%, \quad (11)$$

$$P(\alpha_s - 10^\circ < \alpha < \alpha_s + 10^\circ) \approx 99.7\%, \quad (12)$$

$$P(\beta_s - 10^\circ < \beta < \beta_s + 10^\circ) \approx 99.7\%, \quad (13)$$

where  $\Delta L_s$  represents a planned anastomosis location and  $\alpha_s, \beta_s$  represent the planned anastomosis angles. Therefore, the uncertainty of anastomosis can be formulated as follows.

$$\Delta L \sim \mathcal{N}(\Delta L_s, \sigma_L^2), \quad (14)$$

$$\alpha \sim \mathcal{N}(\alpha_s, \sigma_\alpha^2), \quad (15)$$

$$\beta \sim \mathcal{N}(\beta_s, \sigma_\beta^2), \quad (16)$$

where  $3\sigma_L = 5 \text{ mm}$ ,  $3\sigma_\alpha = 10^\circ$ , and  $3\sigma_\beta = 10^\circ$ .

### F. Hemodynamic Simulation

We used an open source CFD software package OpenFOAM [20] to compute Fontan hemodynamics. Blood was modeled as an incompressible Newtonian fluid [21] with a density of  $1060 \text{ kg m}^{-3}$  and a dynamic viscosity of  $3.5 \times 10^{-3} \text{ Pas}$ . 3D steady-state Navier-Stokes (NS) equations were solved in the domain of a Fontan model using the SimpleFoam solver. We set the convergence values of the pressure and velocity residuals as  $10^{-4}$ . Massless and infinitesimal particles were released into the IVC to trace hepatic blood flow. The HFD can be represented by the ratio of particle numbers that arrive at LPA ( $N_{\text{LPA}}$ ) and RPA ( $N_{\text{RPA}}$ ):

$$\text{HFD}_{\text{LPA}} = \frac{N_{\text{LPA}}}{N_{\text{LPA}} + N_{\text{RPA}}}. \quad (17)$$

iPL and %WSS were calculated based on (1), (2), and the solved computation domain.  $\bar{p}_I, \bar{p}_O, \bar{u}_I$  and  $\bar{u}_O$  in (1) were measured using cross-sectional average values at inlets and outlets. Refer to [12] for more details on our hemodynamic simulation setup. The hemodynamic parameters highlighted in red in Fig. 3 were considered beyond the threshold.

## III. RELIABILITY-BASED ROBUST OPTIMIZATION FRAMEWORK

### A. Overview of Computation Framework

The RBRO framework consists of four main components, as shown in Fig. 4: (A) framework input; (B) Fontan pathway parameterization; (C) surrogate model generation for hemodynamic parameters; and (D) optimization of Fontan pathways. 3D patient-specific models were preprocessed to remove existing Fontan pathways for new graft planning. The pre-operative BC include the percentage of outflow to the LPA  $F_{\text{LPA}}$ , inlet flow rates  $Q_{\text{IVC}}$  and  $Q_{\text{SVC}}$ , and the estimated post-operative BC  $Q'_{\text{IVC}}, Q'_{\text{SVC}}, Q'_{\text{LPA}}$  and  $Q'_{\text{RPA}}$ . The Fontan pathway parameterization defines the design space of the grafts to explore various surgical plans. Computing the hemodynamic parameters directly from high-fidelity simulations is computationally expensive, which makes the optimization process formidable. Surrogate models of high-fidelity hemodynamic simulation significantly reduce computation time while preserving prediction accuracy.

By taking the graft design space, surrogate models, and uncertainty models as input, we developed a two-step optimization strategy, including a DO step and an OUU step, to explore the reliability and robustness of Fontan graft designs.

### B. Fontan Conduit Parameterization

We created a 10-dimensional design space to parameterize a patient-specific Fontan conduit in our previous study [12] as shown in Fig. 4(B). The design parameters  $\mathbf{x} = \{a, b, \alpha_s, \beta_s, \Delta L_s, D_{12}, D_{45}, v_1, v_2, \theta\} \in \mathbb{R}^{10}$ . The conduit pathway is defined by a fourth-order Bézier curve, whose shape is controlled by spatial points  $\mathbf{P}_1(\Delta L_s), \mathbf{P}_2(\Delta L_s, \alpha_s, \beta_s, D_{12}), \mathbf{P}_3(v_1, v_2, \theta), \mathbf{P}_4(D_{45}), \mathbf{P}_5$ .  $a$  and  $b$  define the ellipse radii of the conduit that connects to the superior cavopulmonary connection (SCPC).  $\alpha_s$  and  $\beta_s$  define the spatial direction of  $\mathbf{P}_1\mathbf{P}_2$ , which determines the angle of anastomosis.  $\Delta L_s$  defines the  $\mathbf{P}_1$  location (ellipse center) on the centerline of the PA.  $D_{12}$  and  $D_{45}$  represent the distances (coefficients of a pre-determined maximum distance) of  $\mathbf{P}_1\mathbf{P}_2$  and  $\mathbf{P}_4\mathbf{P}_5$ , respectively.  $v_1, v_2$  and  $\theta$  define the location of  $\mathbf{P}_3$ .  $v_1$  is the Euclidean distance from  $\mathbf{P}_3$  to the vector  $\mathbf{P}_5\mathbf{P}_4$ .  $v_2$  is the distance from  $\mathbf{P}_3$  to the cutting surface of IVC.  $\theta$  is the azimuth angle between a reference direction and the projected line of  $\mathbf{P}_3\mathbf{P}_5$  on the IVC cutting plane. The 3D conduit generation method is detailed in [12].

### C. Surrogate Model Generation

To reduce computational cost for evaluate hemodynamic performance and graft implantation feasibility of various conduit designs, Gaussian process regression with radial-basis functions (RBFs) was used to generate surrogate models for HFD, iPL, %WSS. To eliminate infeasible Fontan pathways that have significant geometrical interference with the heart or have unsmooth graft surface construction, we introduce two additional metrics to measure the geometrical interference depth (InDep) and conduit model quality (Nv). The detailed algorithms are documented in [12]. Maximum Likelihood Estimation (MLE) is used to find the optimal values of the hyperparameters of the RBFs governing the trend and correlation functions. In addition to the 10 design parameters  $\mathbf{x}$ , two uncertainty variables of BC  $F_{\text{LPA}}$  and  $Q_{\text{IVC}}$  are added as input arguments for the surrogate models. By representing

$$\mathbf{x}' = [\mathbf{x}, F_{\text{LPA}}, Q_{\text{IVC}}], \quad (18)$$

the surrogate models are formulated as

$$f_e(\mathbf{x}') = \hat{\zeta}_e + \mathbf{c}_e^T(\mathbf{x}')\mathbf{C}_e^{-1}(\hat{\mathbf{f}}_e - \hat{\zeta}_e\mathbf{f}), \quad (19)$$

where  $e = \{\text{iPL}, \text{HFD}_{\text{LPA}}, \text{\%WSS}, \text{Nv}, \text{InDep}\}$ ,  $\mathbf{C}_e$  is the covariance matrix,  $\mathbf{c}_e(\mathbf{x}')$  is the covariance vector,  $\hat{\mathbf{f}}_e$  is the training data vector.  $\mathbf{f}$  is a unity vector.  $\hat{\zeta}_e$  is the generalized least squares estimate of the mean response [22].

In our prior studies, we have validated the accuracy of the surrogate models [12] based on the 10-dimensional design space and the accuracy of the high-fidelity CFD simulations [10] using *in vitro* experiment. The results indicated that 2000~3000 training samples can provide a good trade-off between the accuracy of the surrogate prediction and the training data scale. Latin hypercube sampling (LHS) [23] was used to efficiently sample

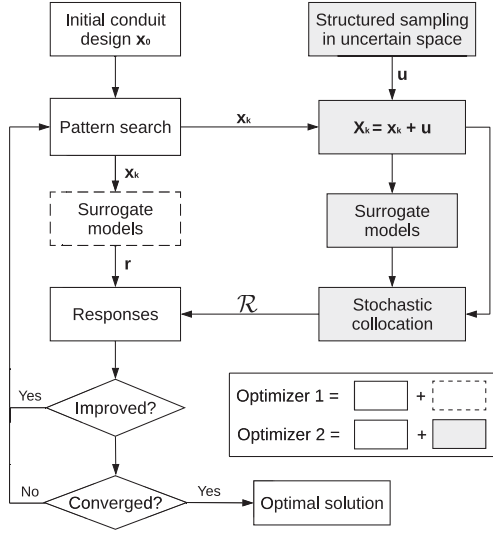


Fig. 6. Block diagram of the optimizer 1 and the optimizer 2. The optimizer 1 represents the DO process, which does not consider the uncertainty of BC and anastomosis. The optimizer 2 performs uncertainty quantification (UQ) with the uncertainty space  $\mathbf{u}$  on each set of explored design parameters  $\mathbf{x}_k$  to generate statistic responses of the hemodynamic parameters.

$\mathbf{x}'$ . Although two additional parameters are added in this study, the cross-validation results for the surrogate models with 12 input parameters demonstrated accuracy similar to the results for the surrogate models with 10 design parameters.

#### D. Optimization

We aim to compute Fontan conduits that can resist the influence of the uncertainties of BC and anastomosis displacements to satisfy the thresholds of Fontan hemodynamics presented in Section II-B4. Because HFD is the most sensitive Fontan hemodynamic parameter in the presence of uncertainties, the objective of Fontan conduit optimization is to search for conduit design parameters that maximize the probability of  $\text{HFD}_{\text{balanced}}$ .

**1) Optimization Strategy:** To search for globally optimal solutions under uncertainty, an intuitive optimization strategy is to first sample a sufficient number ( $N = 600$  [12]) of initial guesses distributed in the design space. Starting from each initial guess  $\mathbf{x}_0$  as shown in Fig. 6, an optimizer then searches in different directions and generates a new  $\mathbf{x}_k$  in the  $k^{\text{th}}$  iteration with the maximum number of iterations  $K$ . This uncertainty quantification (UQ) process generates  $M$  samples in the uncertainty space. Combining with the design parameters  $\mathbf{x}_k$ , the statistics of the response functions  $\mathbf{S}_{\mathcal{R}}$  can be computed. Assuming  $M = 100$ ,  $K = 200$ , the total number of simulations is approximately  $N \times M \times K = 12,000,000$ . Each simulation will generate a separate file (for parallel computation) to record a sampled set of design parameters and their corresponding hemodynamic parameters, as well as other values of constraint parameters. The file system of our high-performance computing cluster is restricted to store a significantly lower number of files. To improve the computational efficiency, an alternative optimization strategy is to employ DO to compute optimal

solutions as warm starts for OOU. Let us say that we select the top-ranked solutions from DO  $n = 10$ . The total number of simulations is  $N \times K + n \times K \times M = 320,000$ , which is 37.5 times more efficient than the first strategy. The convergence criterion is defined as the change in the objective function in the last 10 iterations with the convergence tolerance of  $10^{-6}$ . Fig. 4(D) shows the optimization workflow. The first optimizer solves the DO problem, and the second optimizer solves the OOU problem with warm starts from DO.

**2) Optimizer 1–Deterministic Optimization:** Optimizer 1 shown in Fig. 4(D) and detailed in Fig. 6 performs DO on a set of initial conduit designs ( $N = 600$ ) generated by the LHS method. The DO problem is formulated as follows:

$$\begin{aligned} \min_{\mathbf{x} \in \mathcal{D}_{\mathbf{x}}} & \quad |f_{\text{HFD}_{\text{LPA}}}(\mathbf{x}, F_{\text{LPA}}, Q_{\text{IVC}}) - 0.5| \\ \text{s.t.} & \quad f_{\text{iPL}}(\mathbf{x}, F_{\text{LPA}}, Q_{\text{IVC}}) < 0.03 \\ & \quad f_{\% \text{WSS}}(\mathbf{x}, F_{\text{LPA}}, Q_{\text{IVC}}) < 10\% \\ & \quad f_{\text{InDep}}(\mathbf{x}, F_{\text{LPA}}, Q_{\text{IVC}}) < 2 \text{ mm} \\ & \quad f_{N_v}(\mathbf{x}, F_{\text{LPA}}, Q_{\text{IVC}}) < 2 \\ & \quad \mathbf{x}_L < \mathbf{x} < \mathbf{x}_U \end{aligned} \quad (20)$$

where the objective function aims to find conduit designs with  $\text{HFD}_{\text{LPA}} = 0.5$ ,  $F_{\text{LPA}}$  and  $Q_{\text{IVC}}$  are with deterministic values, the surrogate functions  $f_{\text{HFD}_{\text{LPA}}}$ ,  $f_{\% \text{WSS}}$ ,  $f_{\text{InDep}}$ ,  $f_{N_v}$  are defined in (19), the thresholds in the constraints are defined in Section II-B4,  $\mathbf{x}_L$  and  $\mathbf{x}_U$  are the lower and upper bounds of  $\mathbf{x}$ . We used the asynchronous parallel pattern search (APPS) method [24] to generate new search points  $\mathbf{x}_k$ , as shown in Fig. 6, in the design space to find optimal solutions.

**3) Optimizer 2–Optimization Under Uncertainty:** The best 10 DO solutions are used as warm starts for the optimization formulated as:

$$\begin{aligned} \min_{\mathbf{x} \in \mathcal{D}_{\mathbf{x}}} & \quad -P(0.4 < f_{\text{HFD}_{\text{LPA}}}(\mathbf{x}, F_{\text{LPA}}, Q_{\text{IVC}}) < 0.6) \\ \text{s.t.} & \quad \mathbb{E}(f_{\text{iPL}}(\mathbf{x}, F_{\text{LPA}}, Q_{\text{IVC}})) \leq 0.03 \\ & \quad \mathbb{E}(f_{\% \text{WSS}}(\mathbf{x}, F_{\text{LPA}}, Q_{\text{IVC}})) < 10\% \\ & \quad \mathbb{E}(f_{\text{InDep}}(\mathbf{x}, F_{\text{LPA}}, Q_{\text{IVC}})) < 2 \text{ mm} \\ & \quad \mathbf{x}_L < \mathbf{x} < \mathbf{x}_U \\ & \quad \Delta L, \alpha, \beta, F_{\text{LPA}}, Q_{\text{IVC}} : \text{Normal distribution} \end{aligned} \quad (21)$$

We converted the maximization problem to a minimization problem by adding a minus sign to  $P(0.4 < f_{\text{HFD}_{\text{LPA}}} < 0.6)$ .  $\mathbb{E}(\cdot)$  represents the expectation operator.

In each optimization iteration of optimizer 2 shown in Fig. 6, the uncertainty space

$$\mathbf{u} = [\Delta L, \alpha, \beta, F_{\text{LPA}}, Q_{\text{IVC}}] = [u_1, u_2, u_3, u_4, u_5] \quad (22)$$

is sampled to evaluate the statistics at  $\mathbf{x}_k$ . We employ the stochastic collocation method for uncertainty quantification due to its higher efficiency and faster convergence rate than sampling-based methods [25].

Stochastic collocation (SC) is represented by a Lagrange interpolation function with known coefficients from the sampled uncertain variables  $\mathbf{U} = [\mathbf{u}_1, \mathbf{u}_2, \dots, \mathbf{u}_n]$  ( $n$  represents the

sample number) and their corresponding response vector  $\mathbf{r}$ . We used the Smolyak-type sparse grid method with the grid level at 2 to generate the samples [26]. Defining  $r_i$  as the  $i^{\text{th}}$  element in  $\mathbf{r}$  that represents the response values at the interpolation points, SC is formulated as

$$\mathcal{R}(\mathbf{u}) \cong \sum_{i=1}^n r_i(\mathbf{u}_i) \mathbf{L}_i(\mathbf{u}), \quad (23)$$

where  $\mathbf{L}_i(\mathbf{u})$  is the  $i^{\text{th}}$  Lagrange polynomial:

$$\mathbf{L}_i(\mathbf{u}) = \prod_{k=1, k \neq i}^n \frac{(u_1 - u_1^k)(u_2 - u_2^k) \cdots (u_5 - u_5^k)}{(u_1^i - u_1^k)(u_2^i - u_2^k) \cdots (u_5^i - u_5^k)}, \quad (24)$$

the superscripts of  $u$  represent the sample index, and  $\mathbf{L}_i(\mathbf{u}_j) = \delta_{i,j}$ , and  $\delta_{i,j}$  is the Kronecker Delta.

Moments of (23) can be derived in a closed form:

$$\mu_{\mathcal{R}} = \mathbb{E}(\mathcal{R}) \cong \sum_{i=1}^n r_i \mathbb{E}(\mathbf{L}_i(\mathbf{u})), \quad (25)$$

$$\sigma_{\mathcal{R}} = \mathbb{E}(\mathcal{R}^2) - \mu_{\mathcal{R}}^2 = \sum_{i=1}^n \sum_{j=1}^n r_i r_j \mathbb{E}(\mathbf{L}_i(\mathbf{u})) \mathbb{E}(\mathbf{L}_j(\mathbf{u})) - \mu_{\mathcal{R}}^2. \quad (26)$$

To evaluate the probabilities,  $10^5$  samples were applied to the stochastic expansion in (23). The RBRO framework was implemented based on the Dakota software package [27].

#### IV. RESULTS

In this section, we demonstrate that the RBRO framework can outperform DO in reliability for Fontan surgical planning. We show how different objective functions in DO affect the RBRO results. We compare the reliability and robustness of a manually optimized Fontan conduit with the conduits computed from DO and OUU, and visualize the geometrical differences of the conduit. We also investigate whether Fontan patients with highly unbalanced PA split can benefit from the RBRO framework, because it is challenging to find surgical plans with balanced HFD for these cases.

##### A. Comparison of Results From DO and OUU

We first evaluate the performance of the Fontan conduit designs computed from DO, and compare them with the performance of the conduit designs from OUU to evaluate the effectiveness of the RBRO framework. Fig. 7(A), (B), (C), and (D) show reliability  $P(\text{HFD}_{\text{balanced}})$  of the optimized conduit designs. For each patient case, the top ten designs from DO were selected as warm starts for OUU by ranking the objective function in (20). The rankings of DO solutions are indicated by the circled numbers in Fig. 7(A), (B), (C), and (D) with their associated reliability shown in the gray bars. The red bars represent the reliability of the OUU solutions computed from their corresponding DO solutions.

Since we investigate reliability of the optimized conduit designs, we sorted the original rankings of DO solutions based on their reliability  $P(\text{HFD}_{\text{balanced}})$ , as shown in the x axes of Fig. 7(A), (B), (C), and (D). The reliability of DO solutions

ranges from high to low.  $P(\text{HFD}_{\text{balanced}})$  is estimated by sampling the uncertainty space, as described in Section III-D3. Thus, we name the title of the x axes ‘‘DO solution order ranked by UQ’’.

Fig. 7(A), (B), (C), and (D) demonstrate that the original rankings of DO designs are unable to guarantee their reliability. For certain patients, such as  $F_4$ , the best original DO design has the lowest reliability. The RBRO framework can improve the reliability of DO solutions up to 56.7%, 9.3%, 6.6%, and 79.2% for the four patients, respectively.

Fig. 7(E) demonstrates how  $\text{HFD}_{\text{LPA}}$  changes under uncertain parameters  $\mathbf{u}$  in  $\mathbf{x}_{\text{DO}}^*$  and  $\mathbf{x}_{\text{OUU}}^*$ , which are the optimized design parameters of DO and OUU, respectively. In this example, we compared four conduit designs from the groups #1 (top-ranked DO design) and #10 (best original DO design) in  $F_4$ . In each column of Fig. 7(E), the three rows from top to bottom represent functions of  $\text{HFD}_{\text{LPA}}(F_{\text{LPA}}, Q_{\text{IVC}}, \mathbf{x})$ ,  $\text{HFD}_{\text{LPA}}(\Delta L, \alpha, \mathbf{x})$ , and  $\text{HFD}_{\text{LPA}}(\Delta L, \beta, \mathbf{x})$ . In the contour map, the white color indicates  $\text{HFD}_{\text{LPA}}$  close to or higher than 0.6, and the black color indicates  $\text{HFD}_{\text{LPA}}$  close to or lower than 0.4. OUU solutions  $\mathbf{x}_{\text{OUU}}^*$  exhibit a significantly wider range of  $\text{HFD}_{\text{LPA}}$  within the thresholds than  $\mathbf{x}_{\text{DO}}^*$ , especially for the group #10, by comparing Fig. 7(E-3a) and 7(E-4a), 7(E-3b) and 7(E-4b), and 7(E-3c) and 7(E-4c). The DO solution in the group #1 already provided high reliability of HFD, OUU demonstrates a minor improvement in reliability against  $\alpha, \beta, \Delta L$ , as shown in Fig. 7(E-1b), 7(E-2b), 7(E-1c), and 7(E-2c). However, a small improvement on handling the uncertainty of BC can be observed in Fig. 7(E-1a) and 7(E-2a).

The top-ranked conduit designs from DO and OUU as well as the best original DO designs for the four patients are presented in Table I. The top-ranked design parameters of DO and OUU are different in the size of the conduit ( $F_1, F_2, F_4$ ), the angle of anastomosis ( $F_2, F_4$ ), the location of the anastomosis ( $F_1$ ). The best original DO designs have lower reliability and higher iPL robustness in iPL than those of the top-ranked DO designs. Here, we provide a direct comparison of hemodynamic metrics between native Fontan conduits and the top-ranked OUU designs:  $F_1$ –{ $\text{HFD}_{\text{LPA}}$  (31%, 52.8%), iPL (0.042, 0.023), %WSS (0.4%, 0.98%)};  $F_2$ –{ $\text{HFD}_{\text{LPA}}$  (36%, 53.4%), iPL (0.031, 0.019), %WSS (0.6%, 2.83%)};  $F_3$ –{ $\text{HFD}_{\text{LPA}}$  (72%, 48.3%), iPL (0.008, 0.014), %WSS (12%, 0.91%)};  $F_4$ –{ $\text{HFD}_{\text{LPA}}$  (71%, 50.9%), iPL (0.011, 0.014), %WSS (59%, 3.8%)}, where the first values in the parentheses are from the native conduits, and the second values are from the top-ranked OUU designs.

Fig. 8 shows that the top-ranked DO and OUU conduit designs, which are represented in gray and red, respectively. Similar design parameters lead to comparable hemodynamic performance with 0%~4% improvements on  $P(\text{HFD}_{\text{balanced}})$ , 0%~9.4% improvements in  $\mathbb{E}(\text{iPL})$  using the RBRO framework.

##### B. OUU With Different Objective Function in DO

We formulated the optimizer 1 by optimizing HFD in the objective function (20) for the RBRO framework. We are interested in studying the influence of using a different DO formulation,

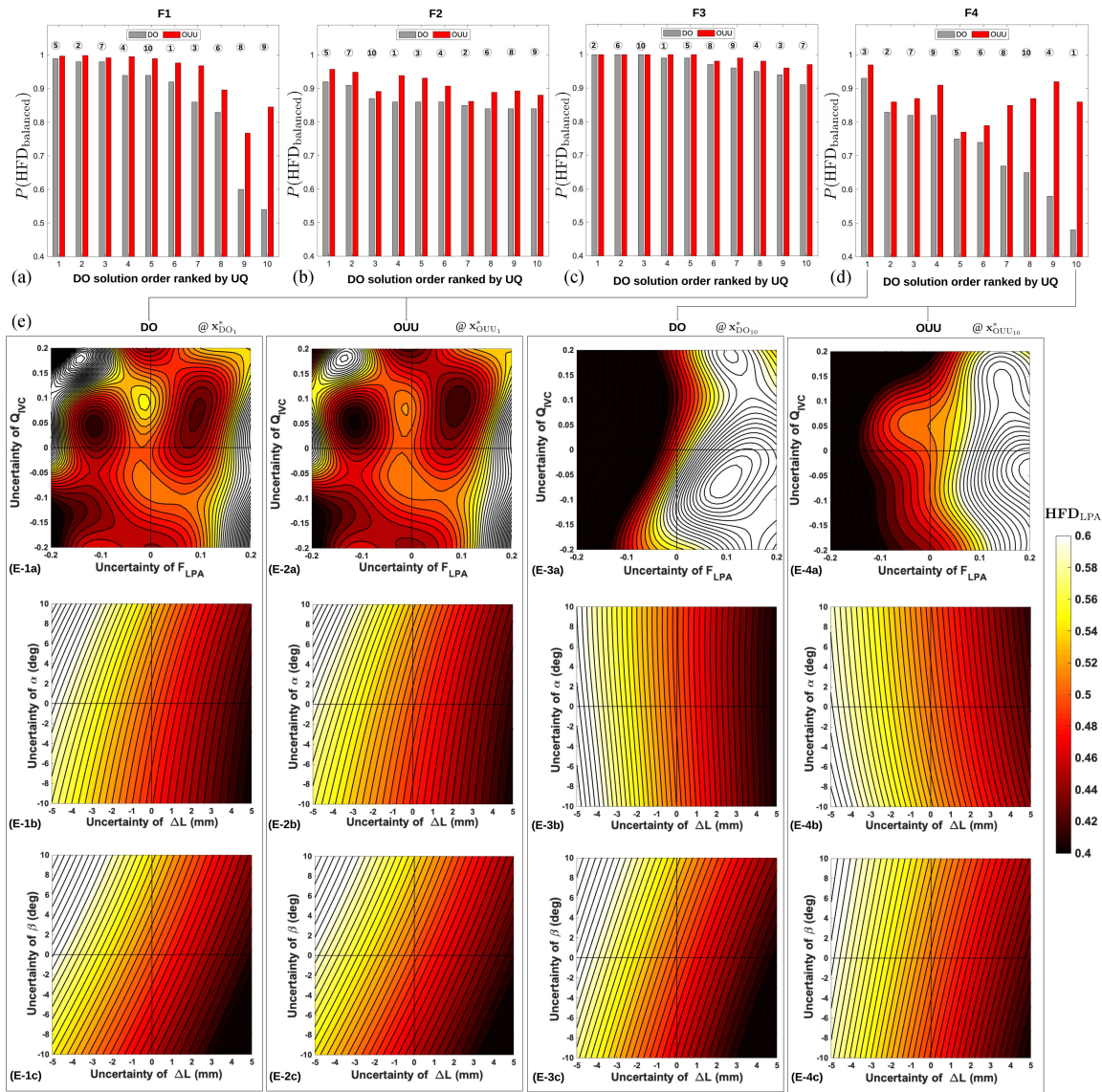


**Fig. 7.** The probability of having balanced HFD  $P(\text{HFD}_{\text{balanced}})$  of optimized graft designs by using deterministic optimization (DO) and optimization under uncertainty (OUU) methods for each patient. The result for the patient  $F_1$  is shown in (A). The y-axis represents the probability of  $\text{HFD}_{\text{LPA}}$  within the thresholds. The x-axis represents DO design order ranking from the most reliable HFD to the least reliable HFD by using UQ. The 10 DO designs are the warm starts for OUU. The circled numbers above the bars represent the original ranking of the DO designs according to the objective function of (20). The same analysis for the patients  $F_2$ ,  $F_3$  and  $F_4$  are shown in (B), (C), and (D), respectively. (E) illustrates how the uncertain parameters  $\mathbf{u}$  affect  $\text{HFD}_{\text{LPA}}$  for the optimized designs in the groups #1 and #10 of  $F_4$ . The three rows show  $\text{HFD}_{\text{LPA}}(F_{\text{LPA}}, Q_{\text{IVC}}, \mathbf{x})$ ,  $\text{HFD}_{\text{LPA}}(\Delta L, \alpha, \mathbf{x})$ ,  $\text{HFD}_{\text{LPA}}(\Delta L, \beta, \mathbf{x})$ .  $\mathbf{x}$  represents the graft design parameters  $\mathbf{x}_{\text{DO}_1}^*$ ,  $\mathbf{x}_{\text{OUU}_1}^*$ ,  $\mathbf{x}_{\text{DO}_{10}}^*$ ,  $\mathbf{x}_{\text{OUU}_{10}}^*$  in the four columns, respectively. Note:  $\text{HFD}_{\text{LPA}} > 0.6$  is represented by white color, and  $\text{HFD}_{\text{LPA}} < 0.4$  is represented by black color.

**TABLE I**  
DESIGN PARAMETERS AND FONTAN HEMODYNAMIC RESPONSES OF OPTIMAL DESIGNS. TOP-RANKED DO DESIGN, TOP-RANKED OUU DESIGN, AND THE BEST ORIGINAL DO DESIGN FOR EACH PATIENT ARE PRESENTED

Optimal designs	Design parameters										Responses		
	a (mm)	b (mm)	$\alpha_s$ (rad)	$\beta_s$ (rad)	$\Delta L_s$	$D_{12}$	$D_{45}$	$v_1$ (mm)	$v_2$ (mm)	$\theta$ (rad)	$P(\text{HFD}_{\text{balanced}})$	$\mathbb{E}(\text{IPL})$	$\mathbb{E}(\% \text{WSS})$ (%)
$F_1$ , top-ranked DO	12.29	10.44	1	-0.66	85.54	1	1	40.74	14.67	3.37	0.99	0.026	0.97
$F_1$ , top-ranked OUU	11.44	10.02	1	-0.66	84.50	1	0.75	40.74	14.67	3.37	1	0.023	0.98
$F_1$ , best original DO	10.23	7.77	0.45	-0.52	86.32	0.30	0.92	21.79	38.05	3.83	0.92	0.028	1.62
$F_2$ , top-ranked DO	7.35	9.57	0.76	-0.03	186.36	0.36	0.98	39.62	17.57	5.15	0.92	0.022	3.05
$F_2$ , top-ranked OUU	8.49	10	0.01	0.53	186.36	0.30	0.85	39.62	17.27	5.35	0.96	0.019	2.83
$F_2$ , best original DO	9.84	7.57	1	-0.38	166.54	1	0.25	38.82	11.60	1.02	0.86	0.017	2.63
$F_3$ , top-ranked DO	8.61	10	1	-0.06	73.11	1	0.48	37.99	35.89	4.36	1	0.014	0.91
$F_3$ , top-ranked OUU	8.61	10	1	-0.06	73.11	1	0.48	37.99	35.89	4.36	1	0.014	0.91
$F_3$ , best original DO	7.82	6.99	0.64	-0.26	58.21	0.48	0.21	44.60	29.38	4.07	0.99	0.024	0.76
$F_4$ , top-ranked DO	8.32	9.65	0.96	0.03	146.37	0.57	0.47	46.75	22.85	3.28	0.93	0.015	3.5
$F_4$ , top-ranked OUU	8.32	10.65	1	0.03	146.37	0.57	0.47	46.75	22.85	3.28	0.97	0.014	3.8
$F_4$ , best original DO	8.85	9.11	0.79	-0.93	127.01	0.1	1	8.89	21.99	0.96	0.48	0.018	5.5



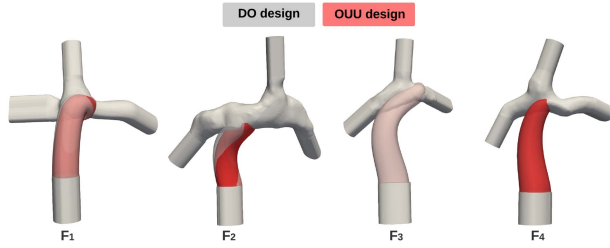


**Fig. 8.** Illustration of the top-ranked DO and OUU designs for the 4 patients. It is hard to tell the geometrical differences between DO and OUU designs for  $F_3$  and  $F_4$ , because the design parameters are identical for DO and OUU in  $F_3$  (see Table I) and the graft diameter of the OUU design in  $F_4$  is slightly larger than that of the DO design with all the other design parameters almost the same.

i.e., minimizing iPL as the objective function:

$$\begin{aligned}
 & \min_{\mathbf{x} \in \mathcal{D}_{\mathbf{x}}} f_{\text{iPL}}(\mathbf{x}, F_{\text{LPA}}, Q_{\text{IVC}}) \\
 & \text{s.t. } 0.4 < f_{\text{HFD}_{\text{LPA}}}(\mathbf{x}, F_{\text{LPA}}, Q_{\text{IVC}}) < 0.6 \\
 & f_{\% \text{WSS}}(\mathbf{x}, F_{\text{LPA}}, Q_{\text{IVC}}) < 10\% \\
 & f_{\text{InDep}}(\mathbf{x}, F_{\text{LPA}}, Q_{\text{IVC}}) < 2 \text{ mm} \\
 & f_{N_v}(\mathbf{x}, F_{\text{LPA}}, Q_{\text{IVC}}) < 2 \\
 & \mathbf{x}_L < \mathbf{x} < \mathbf{x}_U
 \end{aligned} \tag{27}$$

Instead of pursuing a perfectly balanced HFD in DO, (27) minimizes iPL while constraining HFD within the threshold.

Fig. 9 demonstrates how the changing of objective function in DO affects the DO and OUU results. We performed this statistical analysis using 80 DO solutions and 80 OUU solutions. Half of the data (40 DO and 40 OUU solutions) are illustrated in Fig. 7(A), (B), (C), and (D), which are based on the original DO formulation (20). The other half of the data was obtained by performing DO with the formulation (27) and feeding warm starts to the OUU for the four patient cases.

Fig. 9(A) and 9(D) compare the reliability of HFD and the robustness of iPL in DO designs with  $\min | \text{HFD}_{\text{LPA}} - 0.5 |$  (red bars) and  $\min \text{iPL}$  (gray bars) as objective functions. We represent the mean and standard deviation of each data group as mean  $\pm$  standard deviation in the following text. Unpaired 2-tailed t-tests were used to compare the results between the red and gray groups. A  $p$ -value  $< .05$  was considered statistically significant. In Fig. 9(A), we found that except for the patient  $F_1$  (red:  $0.86 \pm 0.03$ , gray:  $0.80 \pm 0.03$ ,  $p = 0.49$ ), the red groups statistically perform better than the gray groups. The result for  $F_4$  shows the most significant difference with  $p = 0.00097$  (red:  $0.73 \pm 0.02$ , gray group:  $0.51 \pm 0.01$ ). Although the  $p$  values of the  $F_2$  and  $F_3$  groups were slightly higher than the significance level, the means of the red groups are higher than those of the gray groups, and the standard deviations of the red groups are much lower than those of the gray groups ( $F_2$ : red  $0.87 \pm 0.0008$ , gray  $0.73 \pm 0.04$ ;  $F_3$ : red  $0.91 \pm 0.0009$ , gray  $0.84 \pm 0.03$ ). In Fig. 9(D), the mean iPL of the gray groups is significantly lower than those of the red groups. The results in Fig. 9(A) and 9(D) generally fall within our expectation.

The OUU performance of different DO objective functions shown in Fig. 9(B) is mixed for  $P(\text{HFD}_{\text{balanced}})$ . There were

**TABLE II**  
PERFORMANCE COMPARISON OF CONDUIT DESIGNS FROM MANUAL OPTIMIZATION, TOP-RANKED DO AND TOP-RANKED OUU FOR  $F_2$

Metrics	Manual	DO	OOU
$P(\text{HFD}_{\text{balanced}})$	0.82	0.92	0.96
$\mathbb{E}(\text{iPL})$	0.028	0.022	0.019
$\mathbb{E}(\% \text{WSS})$ (%)	1.4	3.1	2.8

no significant differences between the red and gray groups for patients  $F_1$  ( $p = 0.95$ ) and  $F_3$  ( $p = 0.30$ ). The gray group in  $F_2$  performs significantly better than the red group ( $p = 0.0016$ ). In contrast, the red group performs significantly better than the gray group in  $F_4$  ( $p = 0.0045$ ). In Fig. 9(E) for  $\mathbb{E}(\text{iPL})$ , the gray groups show significantly better performance than the red groups in  $F_3$  ( $p = 0.031$ ) and  $F_4$  ( $p = 0.0009$ ). No significant differences between the red and gray groups are shown in  $F_1$  ( $p = 0.083$ ) and  $F_2$  ( $p = 0.18$ ). According to the results, the OUU algorithm does not have a strong preference for the DO objective function.

To demonstrate the effectiveness of the RBRO framework, we combined the DO and OUU results of all patients to perform a statistical analysis with 80 conduit designs in each group ( $n = 80$ ). Our results indicate that the conduit designs computed from OUU significantly outperform the designs computed from DO for  $P(\text{HFD}_{\text{balanced}})$  with  $p < 0.0001$  and  $\mathbb{E}(\text{iPL})$  with  $p = 0.021$ , as shown in Fig. 9(C) and 9(F).

### C. Comparison of Manually Designed Conduit With DO and OUU Designs

We compare the reliability of a manually performed randomized search for conduit design with the best DO and OUU conduit designs for patient case  $F_2$ . The manual conduit design procedure involves creating a spectrum of conduit models using CAD software and evaluating them using CFD software. The conduit with the best performance was selected to manually generate a new group of conduit designs in the next iteration. Three iterations were used to select the best conduit design [11].

To measure  $P(\text{HFD}_{\text{balanced}})$ ,  $\mathbb{E}(\text{iPL})$ , and  $\mathbb{E}(\% \text{WSS})$  for manual conduit design, we generated a parameterized duplicate by minimizing the geometrical difference between the conduits, as shown in Fig. 10(A). In Fig. 10(B) and 10(C), we compare the manually optimized conduit with DO design and OUU design, respectively. As shown in Table II, the manually optimized conduit exhibits the lowest reliability in HFD and the highest iPL while the OUU design demonstrates a 14% improvement on  $P(\text{HFD}_{\text{balanced}})$ . The OUU design also shows the lowest mean iPL among the three designs.

### D. OUU for Patients With Highly Unbalanced $F_{\text{LPA}}$

It is not always feasible to design Fontan conduits with  $\text{HFD}_{\text{LPA}} = 0.5$  if the patient has a highly unbalanced PA split  $F_{\text{LPA}}$ . We are interested in investigating the performance of the RBRO framework for applying to these extreme cases.

$\text{HFD}_{\text{LPA}}$  can be reformulated by:

$$\text{HFD}_{\text{LPA}} = \frac{F_{\text{LPA}}(Q_{\text{IVC}} + Q_{\text{SVC}}) - S_{\text{LPA}}Q_{\text{SVC}}}{Q_{\text{IVC}}} \tag{28}$$

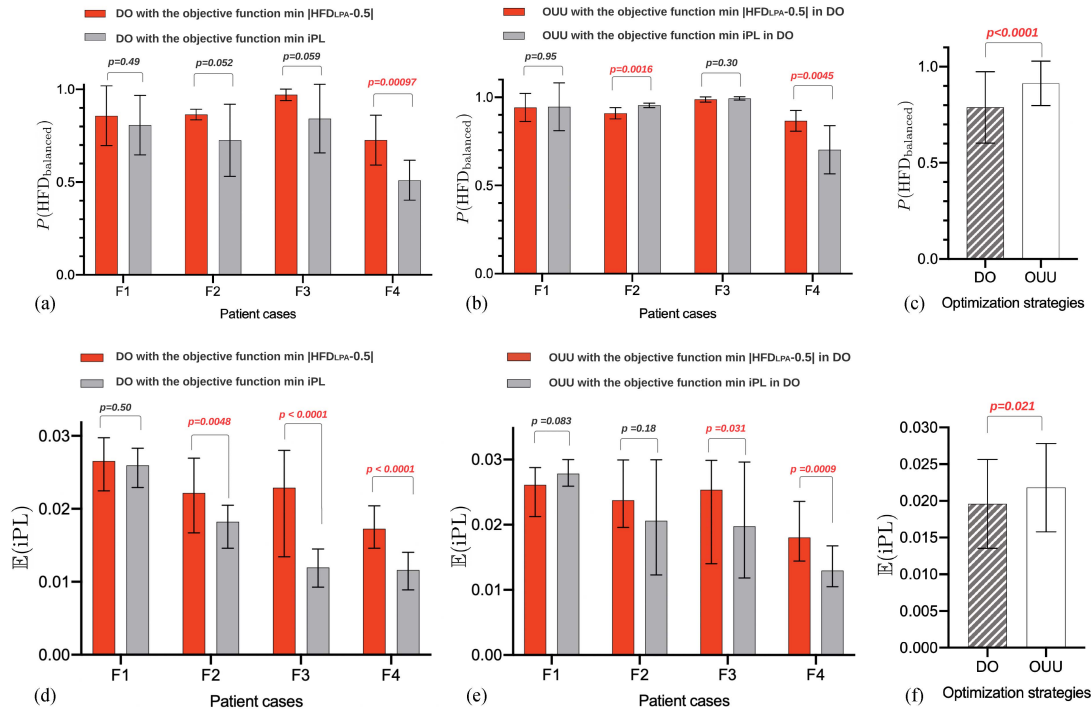


**Fig. 9.** Effect of changing the objective function in DO as minimizing iPL. (A) HFD reliability comparison between DO designs computed from the objective functions  $\min |HFD_{LPA} - 0.5|$  and  $\min iPL$ . (B) HFD reliability comparison between OUU designs computed from the two different objective functions in DO. (C) HFD reliability comparison between DO and OUU designs. (D)  $\mathbb{E}(iPL)$  comparison between DO designs computed from the two different objective functions in DO. (E)  $\mathbb{E}(iPL)$  comparison between OUU designs computed from the two different objective functions in DO. (F)  $\mathbb{E}(iPL)$  comparison between DO and OUU designs. A  $p < 0.05$  is considered statistically significant.

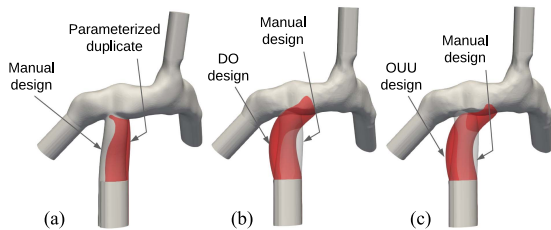


**Fig. 10.** Illustration of Fontan grafts from manual optimization, DO and OUU. (A) Manually optimized graft duplication by minimizing the geometrical difference with the parameterized graft for the patient  $F_2$ . (B) Comparison between the top-ranked DO design and the manually optimized design for  $F_2$ . (C) Comparison between the top-ranked OUU design and the manually optimized design for  $F_2$ .

where  $F_{LPA}(Q_{IVC} + Q_{SVC})$  represents the venous flow rate to the LPA,  $S_{LPA}Q_{SVC}$  represents the flow from the SVC to the LPA. The best  $HFD_{LPA}$  can be found by varying the fraction  $S_{LPA}$  from 0 to 1 [28].

**Fig. 11** visualizes the best possible  $HFD_{LPA}$  by giving a specific  $F_{LPA}$  and the percentage of IVC flow in the total systemic venous flow  $Q_{IVC}/(Q_{IVC} + Q_{SVC})$  based on (28). We use 0.5~0.8 as the range of  $Q_{IVC}/(Q_{IVC} + Q_{SVC})$  to represent the spectrum from pediatric patients to adult patients. The red, white, and blue regions indicate that the best  $HFD_{LPA}$  is higher than 0.5, equal to 0.5, and lower than 0.5, respectively. We marked the locations of the four patient cases in **Fig. 11** according to their BC. It shows that the best theoretical  $HFD_{LPA}$  for  $F_1$ ,  $F_3$ , and  $F_4$  are 0.5. Although  $F_2$  is at the boundary line with a value slightly higher than 0.5, we were able to compute conduit designs with

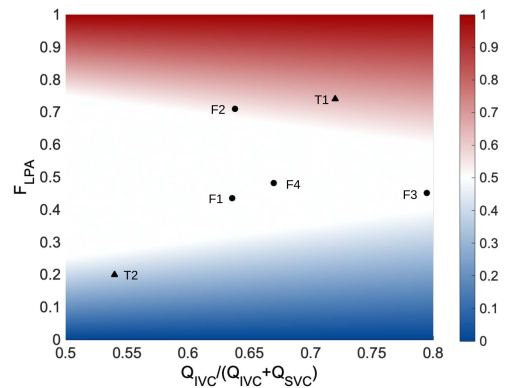


**Fig. 11.** The feasibility of designing grafts with  $HFD_{LPA} = 50\%$  under different patients' blood flow conditions. The x-axis represents the percentage of  $Q_{IVC}$  in the total systemic venous flow ( $Q_{IVC} + Q_{SVC}$ ). The range 0.5~0.8 represents the patient spectrum from pediatric to adult. The y-axis represents  $F_{LPA}$ . The  $HFD_{LPA}$  map is calculated by using (28). The locations of  $F_1$ ,  $F_2$ ,  $F_3$ , and  $F_4$  correspond with their pre-operative BC.  $T_1$  and  $T_2$  represent two extreme cases with highly unbalanced PA flow splits.

$HFD_{LPA} = 0.5$  most likely due to the imperfection of the Lagrangian particle tracking algorithm for the HFD computation. To prepare extreme cases with highly unbalanced  $F_{LPA}$ , we used the Fontan geometry of  $F_1$  and changed its original BC to the values indicated in  $T_1$  ( $F_{LPA} = 0.74$ ,  $Q_{IVC}/(Q_{IVC} + Q_{SVC}) = 0.72$ ) and  $T_2$  ( $F_{LPA} = 0.2$ ,  $Q_{IVC}/(Q_{IVC} + Q_{SVC}) = 0.54$ ).

**Fig. 12** shows the DO (black dots) and OUU (red dots) results for  $T_1$  and  $T_2$ . The dashed lines indicate the DO solutions

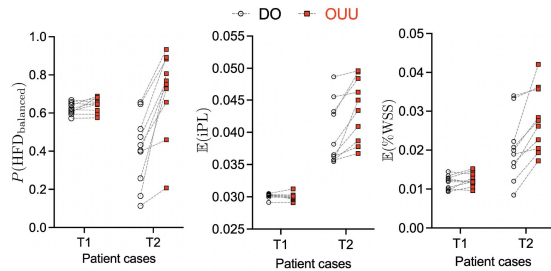


Fig. 12. Fontan graft optimization results for the patient cases  $T_1$  and  $T_2$  with highly unbalanced PA flow splits. Each black dot represents an optimized graft design that was computed from DO. Each red dot represents an optimized graft design that was computed from OUU with a DO solution as a warm start. The dash lines indicate that specific DO designs were used for OUU computation.

from which the OUU solutions were computed. As shown in Fig. 12(A), OUU can hardly improve conduit designs based on DO solutions for  $T_1$  even though the  $P(\text{HFD}_{\text{balanced}})$  values are below 0.7. But for  $T_2$ , OUU significantly improves the reliability of the conduit designs compared to the DO results. We also noticed that all conduit designs produce a much higher power loss (exceeded the 0.03 iPL threshold) in  $T_2$ . It indicates that no feasible solution was found for  $T_2$ . There is a slight concern about %WSS, since all values are far below the 0.1 threshold.

## V. DISCUSSION

Optimization strategies based on the concept of robustness and reliability have been widely applied in the design of engineering systems under uncertainty [29]. In cardiovascular engineering, the impact of BC uncertainty and vessel geometries was investigated for coronary blood flow simulations using uncertainty quantification (UQ) [30]. Different sampling-based strategies were investigated to reduce the computation cost of the UQ of cardiovascular systems [19], [31]. Despite advances in UQ for cardiovascular simulation and deterministic optimization (DO) for surgical planning, it is necessary to develop a patient-specific cardiovascular graft design that considers various sources of uncertainty and automatically computes optimal surgical plans for surgeons to balance hemodynamic performance, robustness, and reliability.

Virtual surgical planning for Fontan graft implantation involves predicting post-operative outcomes and searching for optimal patient-specific solutions. Uncertainties in the modeling of the cardiovascular system and displacement of the anastomosis significantly affect the performance of the HFD of optimal surgical plans calculated using DO methods [8], [14]. To address this challenge, we developed an RBRO framework by actively taking these uncertainties into account in the Fontan pathway design optimization process and maximizing the probability of keeping HFD within the thresholds for making reliable surgical plans. The study demonstrates that the RBRO framework can significantly improve the reliability of the HFD for optimized Fontan conduits compared to the DO framework ( $p < 0.0001$ ).

In Section IV-A, we found that the DO designs of the Fontan conduits were unable to reliably provide good hemodynamic

performance under uncertainties. We also noticed that the top-ranked DO designs by estimating  $P(\text{HFD}_{\text{balanced}})$  demonstrated comparable reliability to the top-ranked OUU designs in the four patient cases. It is worth noting that this re-ranking process of DO solutions is inherently an OUU procedure. Unlike the complete OUU procedure formulated in (21), finding a top-ranked DO solution by UQ only relies on sorting  $P(\text{HFD}_{\text{balanced}})$  of DO solutions. Although it can significantly reduce the computation cost, there is no guarantee of the robustness of other parameters such as iPL and %WSS due to the bypass of the constrained optimization procedure. Depending on the patient's cardiovascular anatomy and hemodynamic condition, constraining the robustness of hemodynamic parameters, such as iPL, may not be a real concern for some patients (e.g.,  $F_4$  shown in Fig. 7(E)) since most Fontan graft designs have iPLs well below the threshold. However, some patients (e.g.,  $F_1$  shown in Fig. 7(E)) may have much higher chance to receive a graft with a high iPL value ( $>0.03$ ) under uncertain BC and displacement of the anastomosis. In the latter case, we need to be careful about using top-ranked DO solutions.

The cases of  $T_1$  and  $T_2$  in Section IV-D represent Fontan patients with a highly unbalanced flow split of PA. We found that for  $T_1$ , which represents an adult patient with  $Q_{\text{IVC}}/(Q_{\text{IVC}} + Q_{\text{SVC}}) = 0.72$  as shown in Fig. 11, OUU provides little improvement in the reliability of HFD even though the best DO solution of  $T_1$  was below 0.7 due to the highly unbalanced PA flow split. When we checked on the other adult patient case  $F_3$ , the DO and OUU solutions were also close, as shown in Fig. 7(C). The results imply that the dominant systemic venous flow from IVC may reduce the uncertainty of HFD and leave OUU little room to improve the reliability of DO solutions. In contrast, the IVC and SVC flow rates in the  $T_2$  case are close ( $Q_{\text{IVC}}/(Q_{\text{IVC}} + Q_{\text{SVC}}) = 0.54$ ). The flow competition of IVC and SVC not only results in a high PL [32], but can also contribute to the low reliability of the DO design that can be significantly improved by OUU.

The results in Fig. 9 demonstrate that the different objective functions of DO, i.e.,  $\min -P(\text{HFD}_{\text{balanced}})$  and  $\min$  iPL, were not consistently preferred by OUU in different patient cases, most likely, because DO solutions only serve as warm starts for OUU. Depending on how the HFD values are related to the design parameters and the uncertain parameters, the OUU solutions could be adjacent to or far from the initial starts.

As stated in Section II-D, this article focuses on investigating short-term post-operative OUU results, which means that vessel growth, changes in cardiac output, and an increase in  $Q_{\text{IVC}}/Q_{\text{SVC}}$  were not considered in pediatric patients. Due to the lack of data on the uncertain parameters, we assumed that these parameters follow the Gaussian distribution according to previous studies [18], [19]. This study was conducted using data from patients who require Fontan revision. For the typical Stage 3 Fontan procedure, the pre-operative and post-operative BC (short-term measurement) may be significantly different from each other. The BC uncertainty model used in this work needs to be improved using clinical data. Additionally, there is currently a lack of data in the literature that characterize the precision of surgical implantation. In current clinical practice, surgeons rely

on their experience and the use of rulers to identify the location of the anastomosis as prescribed in virtual surgical planning. A future research study will consider patient growth in the optimization of the Fontan pathway for pediatric patients. Quantification of surgical implantation accuracy is also important to demonstrate the level of conduit implantation error in current practice. We plan to evaluate this technology using commercially available grafts in clinical and animal studies.

## VI. CONCLUSION

Virtual surgical planning and optimization of Fontan grafts could help improve the post-operative hemodynamic performance of patients. The uncertainties of post-operative blood flow conditions and graft anastomosis displacement may significantly degrade the performance of prescribed surgical plans that are computed from deterministic patient-specific models. To address this problem, we developed a RBRO framework for patient-specific Fontan surgical planning. The RBRO framework is capable of automatically computing the patient-specific Fontan conduit with the maximum possibility of keeping all hemodynamic parameters, including HFD, iPL, and %WSS, in the clinically acceptable range in the presence of uncertain post-operative BC and anastomosis displacements. We tested the proposed RBRO method on four Fontan models that require revision. Compared to DO conduit designs, the conduit design computed from the proposed method demonstrated significantly improved reliability (up to 79.2%) of HFD, while constraining the mean iPL and %WSS below the threshold. The effectiveness of the proposed method encourages its application to account for more challenging conditions, such as the growth of pediatric patients.

## ACKNOWLEDGMENT

The authors acknowledge the supercomputing resource at the Maryland Advanced Research Computing Center (MARCC) (<https://www.marcc.jhu.edu/>) for providing computational resources for this study.

## REFERENCES

- [1] G. Haas *et al.*, "Extracardiac conduit fontan procedure: Early and intermediate results," *Eur. J. Cardio-Thoracic Surg.*, vol. 17, no. 6, pp. 648–654, 2000.
- [2] C. Stamm *et al.*, "Long-term results of the lateral tunnel fontan operation," *J. Thoracic Cardiovasc. Surg.*, vol. 121, no. 1, pp. 28–41, 2001.
- [3] S. Pashneh-Tala, S. MacNeil, and F. Claeysens, "The tissue-engineered vascular graft—past, present, and future," *Tissue Eng. Part B: Rev.*, vol. 22, no. 1, pp. 68–100, 2016.
- [4] R. H. Khiabani *et al.*, "Exercise capacity in single-ventricle patients after fontan correlates with haemodynamic energy loss in TCPC," *Heart*, vol. 101, no. 2, pp. 139–143, 2015.
- [5] N. Pike *et al.*, "Regression of severe pulmonary arteriovenous malformations after fontan revision and "hepatic factor" rerouting," *The Annals Thoracic Surgery*, vol. 78, no. 2, pp. 697–699, 2004.
- [6] K. Pekkan and E. A. B. Whited, "Patient-specific surgical planning and hemodynamic computational fluid dynamics optimization through free-form haptic anatomy editing tool (SURGEM)," *Med. Biol. Eng. Comput.*, vol. 46, pp. 1139–1152, 2008.
- [7] B. Kim *et al.*, "Corfix: Virtual reality cardiac surgical planning system for designing patient specific vascular grafts," in *Proc. 26th ACM Symp. Virtual Reality Softw. Technol.*, 2020, pp. 1–5.
- [8] P. M. Trusty *et al.*, "The first cohort of prospective fontan surgical planning patients with follow-up data: How accurate is surgical planning?," *J. Thoracic Cardiovasc. Surg.*, vol. 157, no. 3, pp. 1146–1155, Mar. 2019.
- [9] D. Siallagan *et al.*, "Virtual surgical planning, flow simulation, and 3-dimensional electrospinning of patient-specific grafts to optimize fontan hemodynamics," *J. Thoracic Cardiovasc. Surg.*, vol. 155, pp. 1734–1742, 2018.
- [10] X. Liu *et al.*, "Computational fontan analysis: Preserving accuracy while expediting workflow," *World J. Pediatr. Congenital Heart Surg.*, vol. 13, no. 3, pp. 293–301, 2022.
- [11] Y.-H. Loke *et al.*, "Role of surgeon intuition and computer-aided design in fontan optimization: A computational fluid dynamics simulation study," *J. Thoracic Cardiovasc. Surg.*, vol. 160, no. 1, pp. 203–212.e2, 2020.
- [12] X. Liu *et al.*, "Semi-automatic planning and three-dimensional electrospinning of patient-specific grafts for fontan surgery," *IEEE Trans. Biomed. Eng.*, vol. 69, no. 1, pp. 186–198, Jan. 2022.
- [13] W. Yang *et al.*, "Hepatic blood flow distribution and performance in conventional and novel y-graft fontan geometries: A case series computational fluid dynamics study," *J. Thoracic Cardiovasc. Surg.*, vol. 143, no. 5, pp. 1086–1097, 2012.
- [14] C. Haggerty *et al.*, "Comparing pre- and post-operative fontan hemodynamic simulations: Implications for the reliability of surgical planning," *Ann. Biomed. Eng.*, vol. 40, pp. 2639–2651, 2012.
- [15] C. M. Haggerty *et al.*, "Fontan hemodynamics from 100 patient-specific cardiac magnetic resonance studies: A computational fluid dynamics analysis," *J. Thoracic Cardiovasc. Surg.*, vol. 148, no. 4, pp. 1481–1489, 2014.
- [16] S. L. Meyerson *et al.*, "The effects of extremely low shear stress on cellular proliferation and neointimal thickening in the failing bypass graft," *J. Vasc. Surg.*, vol. 34, no. 1, pp. 90–97, 2001.
- [17] J. J. Hathcock, "Flow effects on coagulation and thrombosis," *Arteriosclerosis, Thrombosis, Vasc. Biol.*, vol. 26, no. 8, pp. 1729–1737, 2006.
- [18] D. E. Schiavazzi *et al.*, "Uncertainty quantification in virtual surgery hemodynamics predictions for single ventricle palliation," *Int. J. Numer. Methods Biomed. Eng.*, vol. 32, no. 3, 2016, Art. no. e02737.
- [19] S. Sankaran and A. L. Marsden, "A stochastic collocation method for uncertainty quantification and propagation in cardiovascular simulations," *ASME. J. Biomech. Eng.*, vol. 133, no. 3, 2011, Art. no. 031001.
- [20] The OpenFOAM foundation, *OpenFOAM v6*. Accessed: May 3, 2022. [Online]. Available: <https://openfoam.org/version/6/>
- [21] C. G. Caro *et al.*, *The Mechanics of the Circulation*, 2nd ed. Cambridge, U.K.: Cambridge Univ. Press, 2011.
- [22] A. A. Giunta *et al.*, "The surfpack software library for surrogate modeling of sparse irregularly spaced multidimensional data," in *Proc. 11th AIAA/ISSMO Multidisciplinary Anal. Optim. Conf.*, Sep. 2006.
- [23] G. D. Wyss and K. H. Jorgensen, "A user's guide to LHS: Sandia's latin hypercube sampling software," Dept. Risk Assess. Syst. Model., Sandia Nat. Lab., Albuquerque, NM, USA, Tech. Rep. SAND98-0210, 1998.
- [24] P. D. Hough, T. G. Kolda, and V. J. Torczon, "Asynchronous parallel pattern search for nonlinear optimization," *SIAM J. Sci. Comput.*, vol. 23, no. 1, pp. 134–156, 2001.
- [25] M. Eldred, "Recent advances in non-intrusive polynomial chaos and stochastic collocation methods for uncertainty analysis and design," in *Proc. 50th AIAA/ASME/ASCE/AHS/ASC Structures, Struct. Dynamics, Mater. Conf.*, 2009.
- [26] H.-J. Bungartz and M. Griebel, "Sparse grids," *Acta Numerica*, vol. 13, pp. 147–269, 2004.
- [27] B. Adams *et al.*, "Dakota, a multilevel parallel object-oriented framework for design optimization, parameter estimation, uncertainty quantification, and sensitivity analysis: Version 6.12 user's manual," Sandia Tech. Rep. SAND2020-12495, Nov. 2020.
- [28] W. Yang *et al.*, "Optimization of a Y-graft design for improved hepatic flow distribution in the fontan circulation," *J. Biomech. Eng.*, vol. 135, no. 1, 2013, Art. no. 011002.
- [29] E. Acar *et al.*, "Modeling, analysis, and optimization under uncertainties: A review," *Struct. Multidisciplinary Optim.*, vol. 64, pp. 2909–2945, 2021.
- [30] S. Sankaran *et al.*, "Uncertainty quantification in coronary blood flow simulations: Impact of geometry, boundary conditions and blood viscosity," *J. Biomech.*, vol. 49, no. 12, pp. 2540–2547, 2016.
- [31] D. E. Schiavazzi *et al.*, "A generalized multi-resolution expansion for uncertainty propagation with application to cardiovascular modeling," *Comput. Methods Appl. Mechanics Eng.*, vol. 314, pp. 196–221, 2017.
- [32] M. de Leval *et al.*, "Use of computational fluid dynamics in the design of surgical procedures: Application to the study of competitive flows in cavopulmonary connections," *J. Thoracic Cardiovasc. Surg.*, vol. 111, no. 3, pp. 502–513, 1996.